Materials Today Physics 16 (2021) 100299

Contents lists available at ScienceDirect

Materials Today Physics

journal homepage: https://www.journals.elsevier.com/materials-today-physics

Knitting topological bands in artificial sonic semimetals

Li-Yang Zheng [a, 1], Xiu-Juan Zhang [b, 1], Ming-Hui Lu [b, **], Yan-Feng Chen [b], Johan Christensen [a, *]

[a] Department of Physics, Universidad Carlos III de Madrid, ES-28916 Leganès, Madrid, Spain
[b] National Laboratory of Solid State Microstructures and Department of Materials Science and Engineering, Nanjing University, Nanjing, 210093, China

ARTICLE INFO

Article history:
Received 8 September 2020
Received in revised form
1 October 2020
Accepted 2 October 2020
Available online 9 October 2020

ABSTRACT

Frontier investigations on a contemporary family of materials comprise a new class of topological materials that have been discovered in three dimensional (3D) semimetallic crystals. Beyond already unconventional topological quasiparticles in Dirac and Weyl semimetals, nodal-line semimetals provide an even richer platform encompassing robust band-touching manifolds and exotic transport properties. Classical configurations including artificial crystals have emerged as popular systems not only to replicate these new properties in wave-based scenarios, but particularly also to ease experimental complexities of electronic systems and to permit topological tuning via variable geometrical designs. Sonic crystals are one of such example, in which dissimilar fluid or rigid inclusions or channels are combined to tailor the acoustic material response at will. Here, we design a cubic lattice of guiding channels allowing us to map topological characteristics of quasi-particles excitations to audible sound properties. Simply by varying the cross section of these channels, we bring forward multiple phase transitions among four different interlaced nodal features, which resemble the knitting of 3D Bloch-bulk bands in momentum space. One nodal attribute appears to feature an acoustic version of directional massless Dirac fermions, which is experimentally characterized and displays linear crossing in one direction and flat bands in the perpendicular one, enabling strongly focused and collimated sound beams, thanks to this peculiar dispersion.

1. Introduction

The exploration of topological phases of matter has attracted tremendous interests based on novel classifications of materials and appealing transport and waveguiding characteristics [1–6]. Topological insulators (TIs) typically acquire a geometric phase when the degeneracy such as the Dirac point in momentum space is lifted, which leads to the appearance of gapless edge states within the gapped bulk bands [7,8]. Unlike TIs, topological semimetals exhibit gapless bulk bands and the topology is characterized by multiple band degeneracies [9,10]. These band degeneracies are topologically protected by symmetry and can exhibit various features of diverse dimensionalities including the zero-dimensional (0D) nodal points, one-dimensional (1D) nodal lines or rings, and two-dimensional (2D) nodal surfaces [11–16]. The motivation to study the topological properties of these elaborate band manifolds (degeneracies) originates from numerous associated phenomena such as surface Fermi arcs in Weyl semimetals [17], flat drumhead surface states in nodal-line semimetals [18,19], etc. Unravelling new horizons of unprecedented topological phases and related effects, usually requires the existence of unconventional band degeneracies with protected-symmetry [20–24]. Such band-touchings correspond to multiple band crossings of novel quasiparticles carrying different topological charges. Recently, directional massless Dirac fermions have been reported in van der Waals materials, which compared to conventional 2D massless Dirac cones with linear dispersions within the crystal plane, display a remarkable linear directional degeneracy along one path in momentum space, but flat in the perpendicular direction [25]. Such directional Dirac cone (DDC) entails remarkable transport properties thanks to this unusual charge confining dispersion originating from a long-range translational symmetry. Acoustic waves in artificially structured media – a seemingly unrelated area, have lately proven to be a solid base to experimentally test exotic states in otherwise complex

* Corresponding author.
** Correspoding author.
E-mail addresses: luminghui@nju.edu.cn (M.-H. Lu), johan.christensen@uc3m.es (J. Christensen).
[1] These authors contributed equally.

https://doi.org/10.1016/j.mtphys.2020.100299
2542-5293/

electronic settings. Acoustic waves in fluids do not polarize and carry no spin, yet pseudo-spins can be hand-crafted both using metamaterials [26–28] and particularly sonic crystals to emulate the counterpart of massless Dirac quasiparticles for sound in a broad range of experimental realizations at different dimensions [29–32]. It remains however uncharted to observe acoustic directional massless quasiparticles for a spinless system, which thanks to its unique dispersion shape could serve as a topological collimator to direct and focus sound at targeted hotspots.

In this work, we construct a semimetallic crystal for sound waves based on cubic waveguide networks whose topological bands are entirely dictated by the channel cross sections. Thus, multiple interlaced band-touching manifolds are knitted across various topological phases in momentum space, exhibiting quasi-flat acoustic surface states and DDCs. Particularly, the dispersion characteristics of the DDC evoke 3D collimation of sound for audio frequencies. In short, our particular 3D topological design hosts highly complex intersecting nodal features, which permits the deployment of topological functionalities in acoustic devices.

1.1. Knitting interlaced nodal features

In Fig. 1a–d, we classify four different types of interlaced nodal features (INFs). It is shown that the α-type and the β-type INF consist of rings that intersect where two planes cross (cyan and yellow), which originate from the crystalline symmetries, e.g., mirror or glide symmetries. Conversely, when the yellow plane intersects with two cyan planes, the γ-type and the δ-type are formed, resembling a stub-like (Fig. 1c) and a hourglass-like appearance (Fig. 1d), respectively. Figure 1e displays the schematic of the cubic lattice under study. We invoke anisotropy by designing the network of waveguides containing various cross sections, which leads to various hopping strengths t, t',…l' (different color bonds) among neighbouring junctions. Considering an periodic arrangement and using Bloch's theorem, it suffices to regard only the sound pressure at each junction p_A, p_B, …, p_H [see Supporting Information for details]. Hence, the acoustic Hamiltonian for a 3D lattice of waveguides reads

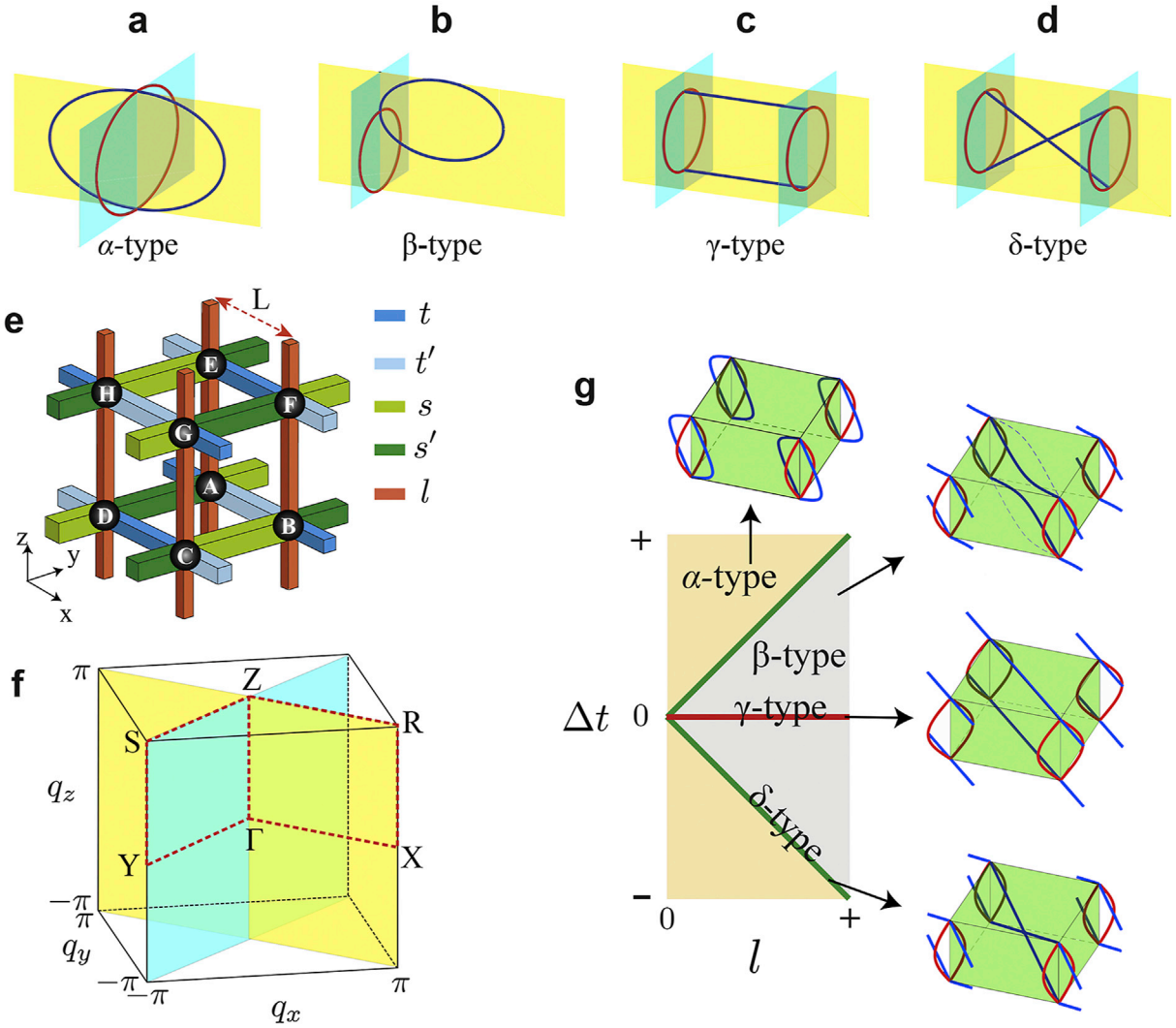

Fig. 1. A catalogue of interlaced nodal lines and stitches as reaped from the cubic waveguide lattice. Schematics of the (a) α-type, (b) β-type, (c) γ-type, and (d) δ-type INFs. (e) Schematic representation of the cubic lattice under study. The air channel geometries are labelled by different colors, while their interconnecting junctions are marked as $A,B,C,\ldots,H$. (f) The BZ with two pseudo-mirror planes marked in yellow and cyan. (g) The existence of four types of INFs in the structure and the corresponding phase diagram.

$$H\begin{bmatrix}\boldsymbol{u}\\ \boldsymbol{v}\end{bmatrix}=\begin{bmatrix}0 & \mathscr{D}\\ \mathscr{D}^{*} & 0\end{bmatrix}\begin{bmatrix}\boldsymbol{u}\\ \boldsymbol{v}\end{bmatrix}=\varepsilon\begin{bmatrix}\boldsymbol{u}\\ \boldsymbol{v}\end{bmatrix}, \tag{1}$$

where $\boldsymbol{u}=[p_A;p_C;p_F;p_H]$, $\boldsymbol{v}=[p_B;p_D;p_E;p_G]$. $\varepsilon=\cos(2\pi f L_e/c)$ is the "energy" term with f the frequency and $c=344\ m/s$ the speed of sound in air. L_e is the effective length of two adjacent junctions, and $\mathscr{D}$ is a 4×4 matrix. The Hamiltonian H has chiral symmetry since there exists a unitary and Hermitian operator $U=[\mathbb{I},0;0,-\mathbb{I}]$ which anti-commutes with the Hamiltonian $UHU=-H$ [33]. For simplicity, we fix the geometrical relation to $t-s=t'-s'=\Delta t$. The structure possesses two translational symmetries along the $m(1,1,0)$ and the $n(1,-1,0)$ directions, leading to their respective operations $T_n=e^{-i(q_x-q_y)/2}$ and $T_m=e^{-i(q_x+q_y)/2}$ due to Bloch's theorem. Thus we can define two pseudo-mirror planes at $q_x\pm q_y=2\pi$ that lead to $T_m=-1$ and $T_n=-1$, which is an important property that can be regarded as an analogy of the Kramers pair [34]. The Brillouin zone (BZ) is shown in Fig. 1f, inside which we identify the two cyan and yellow pseudo-mirror planes. As we will show, band knitting of the nodal features occurs within the two pseudo-mirror planes.

The solutions of Eq. (1) at zero energy lead to the four type of INFs depicted in Fig. 1g, where the green box represents the BZ, in which the blue (red) nodal lines (stitches) reside within the yellow *nz*- (cyan *mz*-) plane of Fig. 1f. The four types of INFs can be transformed into each other by varying the ratio of $\Delta t/l$ as seen in phase diagram presented in Fig. 1g. When $|\Delta t/l|>1$, the crystal acquires an α-type INF. Further, for $|\Delta t/l|=1$, the α-type converts into the δ-type since the two originally separated nodal rings (blue curves) touch each other in the center of the BZ, resulting in a linear nodal crossing. For $|\Delta t/l|<1$, the linear crossing is reopened and the δ-type evolves into the β-type. Lastly, decreasing $|\Delta t/l|=0$, the nodal chain in the *nz*-plane is stretched into a flat Dirac nodal line with four-fold degeneracy at $q_z=\pm\pi$, i.e., the γ-type INF.

The γ-type INF is of particular interests since its dispersion relation allows for the directional flow of sound. In Fig. 2a we show the 3D printed sample of the acoustic semimetallic crystal, with a zoomed view of the unit cell in Fig. 2b. According to the foregone theoretical model, the sample is fabricated with the following coupling coefficients: $t=s\approx0.189$, $t'=s'\approx0.121$, $l\approx0.189$, and $\Delta t=0$. The numerical (circles) and analytical (solid lines) frequency and energy dispersion relations, which reveal a remarkable agreement, display furthermore an array of band-touching manifolds at zero energy, i.e., at $f=7100$ Hz, as seen in Fig. 2c. At this frequency, as shown in Fig. 2d we extract the iso-frequency bands within the green BZ, out of which we are able to separate the INF features, that is, the straight blue nodal lines at the yellow *nz*-plane and the red hyperbolic stitches at the cyan *mz*-plane, which touch

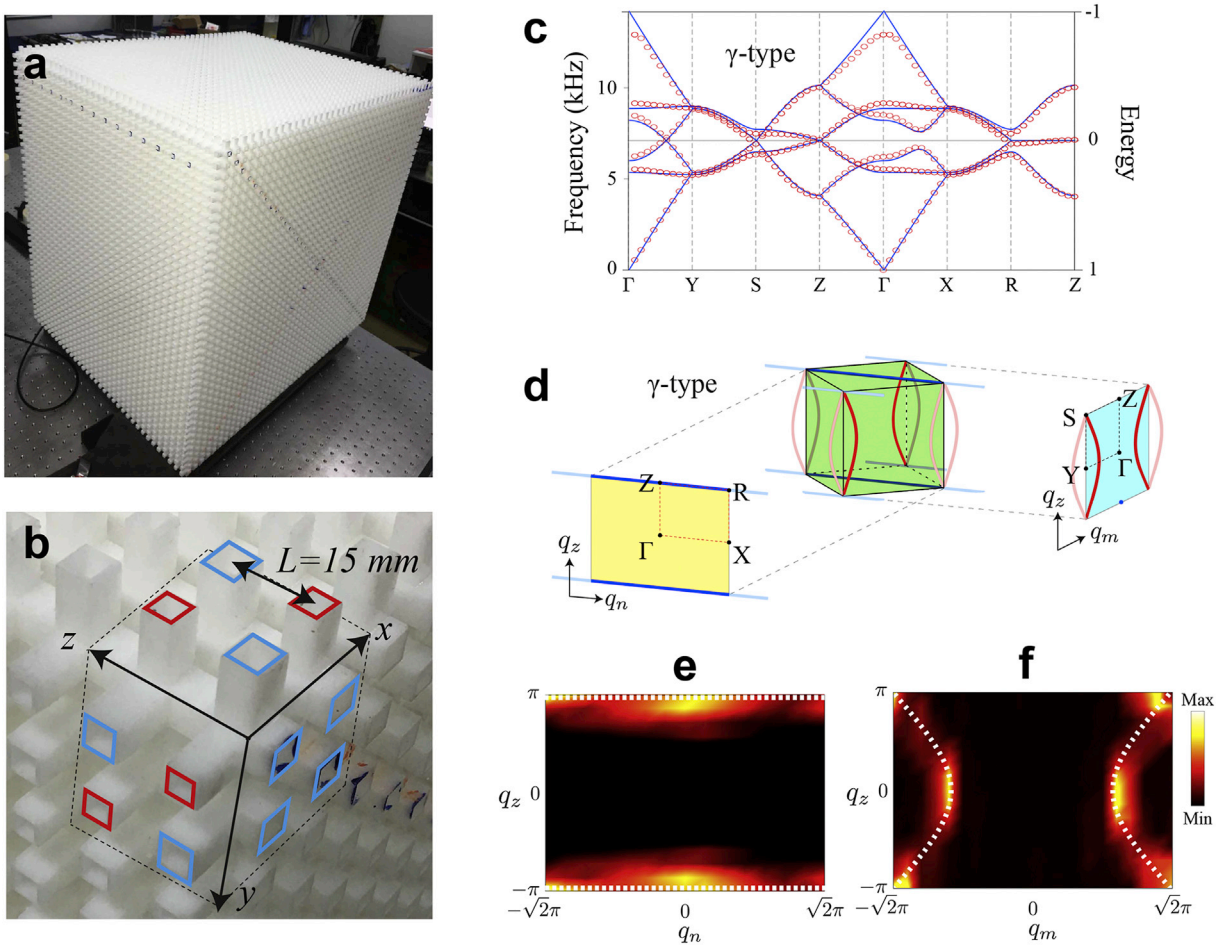

Fig. 2. Experimental observation of interlaced nodal features. (a) A picture of the experimental sample produced by 3D printing. (b) Zoomed view of a unit cell of the sample. The air channels in blue (red) have widths of 5 *mm* (4 *mm*), and the center-to-center distance is $L=15$ *mm*. (c) The corresponding dispersion curves calculated by theory (blue solid lines) and simulation (red circles). (d) Structure of the nodal lines in the BZ (green box). The nodal features (red and blue) are located at two separated mirror planes marked in yellow and cyan. (e)–(f) The measured iso-frequency contours at the two said mirror planes, where q_m, q_n are the normalized wave vector along *m*- and *n*-directions. Color scale indicates the intensity of the states. Dashed lines mark the predicted position of nodal lines.

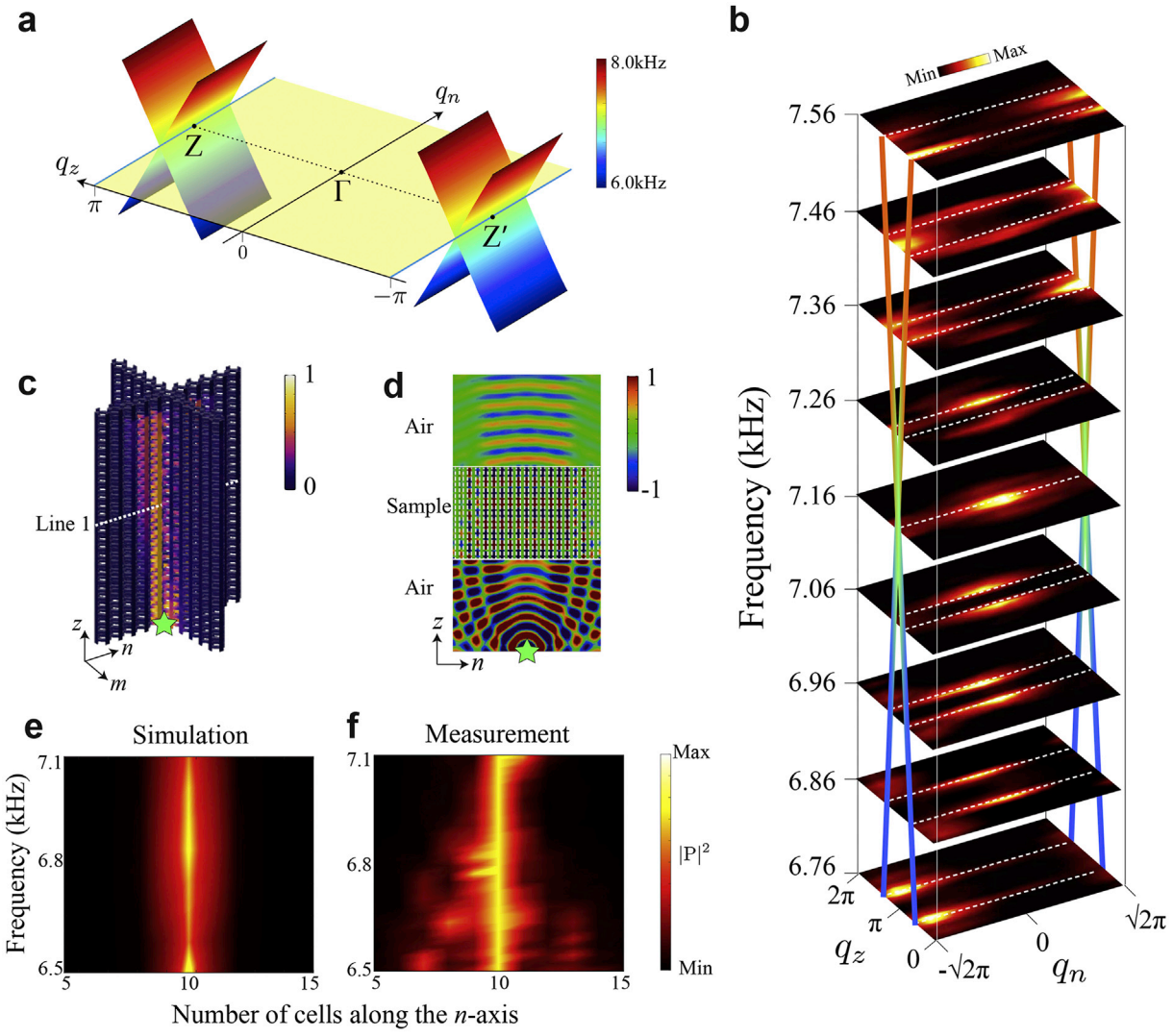

Fig. 3. Experimentally characterized directional Dirac dispersion and sound collimation. (a) 3D view of the directional Dirac cones in the *nz* -plane. Each linear crossing comprises a four-fold degeneracy with flat nodal lines at $q_z = \pm\pi$ (blue). (b) Measured iso-frequency spectrum of the DDC dispersion. The color scale represents the intensity of the states. The dashed white lines mark the predicted position of flat nodal lines. The colored cones correspond to the Dirac dispersion in (a). (c) 3D collimation of sound in response to a point source (green star). (d) Conversion of sound emitted by a free-space point source to outgoing plane waves at 7215 Hz. Simulated (e) and measured (f) sound collimation intensity $|P|^2$ maps, corresponding to the cut "Line 1" in panel (c), as a function of frequency.

at opposite corners of the BZ. By measuring the acoustic pressure at the said frequency across both perpendicular planes within the sample of Fig. 2a, we are able to detect separately the flat nodal lines and the hyperbolic stitches. In concrete, the measured nodal features in the aforementioned *nz*- and *mz*-planes are presented in Fig. 2e-f, respectively. The color scale represents the intensity of the states whereas the dashed lines correspond to the theoretical prediction.

1.2. Directional Dirac cone and sound collimation

Beyond conventional Dirac cones possessing a single 0D point in momentum space where the bands touch, we now expand upon the flat nodal lines running parallel with q_n by considering their frequency dispersion. In doing this, we aim at elucidating the 1D directional massless Dirac counterpart that is pinned along $q_z = \pm\pi$, as seen in Fig. 3a. Experimentally, the DDC is characterised by scanning the acoustic intensity across the *nz*-plane using a frequency sweep around the Dirac frequency. As shown in Fig. 3b, several spectral snapshots from 6.76 to 7.56 kHz have been taken, illustrating how the detected state intensities agree very well with the theoretically predicted ones (white dashed lines). The two crossed and colored (color map in Fig. 3a) lines at two adjacent BZ boundaries render the conical shape of the directional cone. As expected, the measured data confirm clearly that the dispersion relation owns a linear crossing in the q_z direction and flat bands in the perpendicular q_n direction.

The DDC dispersion holds great promise to produce strongly confined and collimated sound beams. Due to the dispersion flatness, sound can hardly escape into its respective direction, while along the *z*-axis, the direction at which the linear crossing is taking place, the acoustic waves flow in a highly directional manner. We put this concept to the test by firstly placing a point source at the lower interface of the cubic crystal. As the simulation in Fig. 3c shows, sound hardly spreads laterally but maintains a strongly collimated shape along *z* as the two orthogonal planes (11×15 cells) depict. Likewise, the DDC dispersion also collimates the emission from a point source to a plane wave. In Fig. 3d we show

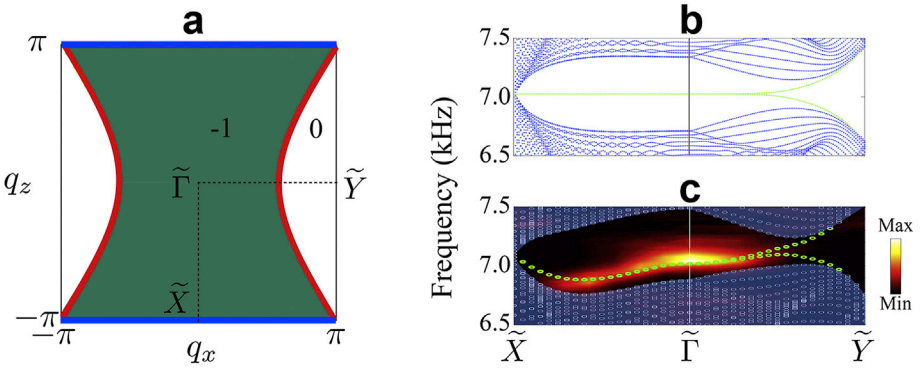

Fig. 4. Predicted and measured quasi-flat acoustic surface states. (a) Winding number $\mathscr{W}$ surface mapping in momentum space, $q_{\parallel} = (q_x, q_z)$. The green (white) region represents the area where $\mathscr{W} = -1$ ($\mathscr{W} = 0$). The red and blue curves are the projections of nodal lines to the surface momentum space. (b) Theoretically obtained projected surface dispersions. The blue lines correspond to the bulk and the green ones to the surface states. (c) Measured (background intensity contour) and numerically simulated (shaded circles) projected bulk bands. The green dots highlight the surface waves dispersion.

the generation of plane waves at 7215 Hz in response to a distant source (green star). Experimentally, we run a frequency scan along the dotted line in Fig. 3c, corresponding to 9 cells deep into the sample. The spectral window ranges from 6.5 to 7.1 kHz as shown in both the simulated (Fig. 3e) and measured (Fig. 3f) data. Both results, with fairly good agreement, illustrate that the acoustic intensity along the indicated path remains highly confined and directional with respect to the DDC dispersion for a rather broad frequency window.

1.3. Quasi-flat surface states

Within the same audible frequency regime, lastly we also demonstrate that the nontrivial topology of the γ-sample gives rise to flat surface states at the $(0, 1, 0)$ crystal termination plane. Due to the existence of chiral symmetry of the Hamiltonian H, the topological invariant of the surface states can be characterized by a winding number [33].

$$\mathscr{W}(q_{\parallel}) = \sum_{j=1}^{h/2} \oint \frac{dq_{\perp}}{2\pi i} \partial_{q_{\perp}} \log D_j, \tag{2}$$

where $h = 8$ is the number of sublattices in the unit cell, $q_{\perp}$ ($q_{\parallel}$) is the vector component perpendicular (parallel) to the surface, and D_j is the complex eigenvalue of the matrix $\mathscr{D}$ in Eq. (1). Thus, the bulk-edge correspondence relates the winding of the system to the number of protected surface states at the terminations. Figure 4a depicts a winding number map within the 2D BZ at zero energy. The winding number $\mathscr{W} = -1$ in the green region (area of the surface states) and is zero in the blank one, in between which, the separations are marked by the projection of the nodal lines at the termination plane, i.e., the red and blue lines. The surface dispersion, as shown in Fig. 4b, is calculated by considering a finite sample (20 cells, more details in the SI), where the green (blue) lines correspond to the surface (bulk) states. The nontrivial region of non-zero winding shown in Fig. 4a, coincides with the location of the surface states. To verify the theory, we conduct both numerical and experimental analysis as shown in Fig. 4c, which appear in good agreement. We observe here that the surface states do not exactly locate at zero energy, i.e., 7100 Hz, but that they are affected by dispersion as compared to the theoretical predictions. This small deviation stems from the fact that the sample operates slightly off the deep subwavelength regime at which the model is valid. Other than that, the observation of topologically protected quasi-flat surface states has convincingly been conducted and might find appealing use for robust slow-sound guiding.

2. Conclusion

By using a cubic lattice of sound guiding channels, we laid the foundation of a tunable acoustic semimetal analogue. Simply by varying the channel cross sections, one is able to tune across several topological phases comprising flat nodal lines, hyperbolic stitches, and the complex knitting of the two. Of particular interest among the landscape of band-touching manifolds, experimentally we unveiled a directional flat Dirac cone, which based on its unusual dispersion profile enables the generation of audible plane waves in response to sound emitted from a distant point source. Beyond the transfer of basic topological concepts in electronics to highly controllable experiments in acoustics, we foresee continuation along this front based on the exploration of analogies and exotic control of sound waves.

2.1. Experimental section

2.1.1. Sample

The sample was fabricated by 3D printing using photosensitive resin. The inner widths of the square channels are 5 *mm* (blue) and 4 *mm* (red). Along the *z*-axis, all channels are 5 *mm* wide (blue). All the channels have a thickness of 1 *mm*. The sample is composed of $20 \times 20 \times 17$ unit cells with an overall dimension of $0.6 \times 0.6 \times 0.51$ *m*. We use a point-like source, which is generated from an acoustic transducer and inserted into the sample through its channels. An acoustic detector (Knowles SPM0687LR5H MEMS microphone with sizes of 4.72 *mm* × 3.76 *mm*) is used to probe the excited pressure field. The data is collected and analysed using a DAQ card (NI PCI-6251).

The γ type INF: The nodal features are measured by scanning separately the sound pressure in the *nz*-and *mz*-planes around the zero energy. The point-like source is inserted at a distance of several unit cells into the sample but slightly off the measured planes. The detector is inserted into the sample through the channels of width 5 *mm* so that the sound pressure at the junctions can be measured. By 2D fast Fourier transforming the signals in the *nz*- and *mz*-planes, we obtain their momentum space contours to map the nodal features in Fig. 2e and f.

Directional Dirac cone: In this experiment, we use the same source as in the previous measurement and scan the field in the *nz*-plane by sweeping a signal from 6.5 kHz to 8.5 kHz.

3D collimation: The source is placed at the bottom center of the sample. In order to clearly detect the sound field by avoiding strong interference near the source, we chose a scanning-line at 9 unit cells into the sample.

Surface waves: The surface is constructed by open ended channels at which we place the source in the center (6.5 kHz−8.5 kHz). Again we conduct Fourier transformations to observe the surface states along the $\tilde{\Gamma}\tilde{X}$ and $\tilde{\Gamma}\tilde{Y}$ directions, as rendered in Fig. 4c.

Credit author statement

J.C. and M.H.L. conceived the idea. L.Y.Z. contributed to the design of the structures and performed the theoretical modeling. X.J.Z. carried out the measurements. L.Y.Z. and X.J.Z. analyzed the experimental data. L.Y.Z. prepared the manuscript. J.C. and M.H.L. supervised all the aspects of the work and managed the project. All the authors contributed to the discussion of the results and the revision of the manuscript.

Declaration of competing interest

The authors declare that they have no known competing financial interests or personal relationships that could have appeared to influence the work reported in this paper.

Acknowledgements

J.C. acknowledges the support from the European Research Council (ERC) through the Starting Grant No. 714577 PHONOMETA and from the MINECO through a Ramón y Cajal grant (Grant No. RYC-2015-17156). X.J.Z. M.H.L. and Y.F.C. acknowledge the support from the National Key R & D Program of China (2017YFA0303702, 2018YFA0306200), the National Natural Science Foundation of China (Grant No. 51902151, 11625418, 11890700, 51732006 and 51902151), the Natural Science Foundation of Jiangsu Province (Grant No. BK20190284) and the Fundamental Research Funds for the Central Universities (14380165).

References

[1] M.Z. Hasan, C.L. Kane, Rev. Mod. Phys. 82 (2010) 3045.
[2] X.-L. Qi, S.-C. Zhang, Rev. Mod. Phys. 83 (2011) 1057.
[3] Y. Ando, L. Fu, Annu. Rev. Condens. Matter Phys. 6 (2015) 361.
[4] N. Armitage, E. Mele, A. Vishwanath, Rev. Mod. Phys. 90 (2018): 015001.
[5] B. Yan, C. Felser, Ann. Rev. Condensed Matter Phys. 8 (2017) 337.
[6] X. Zhang, M. Xiao, Y. Cheng, M.-H. Lu, J. Christensen, Commun. Phys. 1 (2018) 1.
[7] M. Sato, Y. Ando, Rep. Prog. Phys. 80 (2017): 076501.
[8] S. Rachel, Rep. Prog. Phys. 81 (2018) 116501.
[9] M. Ezawa, Phys. Rev. B 96 (2017): 041202.
[10] Z. Yan, Z. Wang, Phys. Rev. Lett. 117 (2016): 087402.
[11] Y. Yang, J.-p. Xia, H.-x. Sun, Y. Ge, D. Jia, S.-q. Yuan, S.A. Yang, Y. Chong, B. Zhang, Nat. Commun. 10 (2019) 1.
[12] S.M. Young, C.L. Kane, Phys. Rev. Lett. 115 (2015) 126803.
[13] L. Lu, Z. Wang, D. Ye, L. Ran, L. Fu, J.D. Joannopoulos, M. Soljačić, Science 349 (2015) 622.
[14] W. Deng, J. Lu, F. Li, X. Huang, M. Yan, J. Ma, Z. Liu, Nat. Commun. 10 (2019) 1.
[15] Q. Yan, R. Liu, Z. Yan, B. Liu, H. Chen, Z. Wang, L. Lu, Nat. Phys. 14 (2018) 461.
[16] M. Hirayama, S. Matsuishi, H. Hosono, S. Murakami, Phys. Rev. X 8 (2018): 031067.
[17] K. Deng, G. Wan, P. Deng, K. Zhang, S. Ding, E. Wang, M. Yan, H. Huang, H. Zhang, Z. Xu, et al., Nat. Phys. 12 (2016) 1105.
[18] Z. Yan, R. Bi, H. Shen, L. Lu, S.-C. Zhang, Z. Wang, Phys. Rev. B 96 (2017): 041103.
[19] A. Merkel, J. Christensen, Commun. Phys. 2 (2019) 1.
[20] Z. Yang, C.-K. Chiu, C. Fang, J. Hu, Phys. Rev. Lett. 124 (2020a) 186402.
[21] C. Gong, Y. Xie, Y. Chen, H.-S. Kim, D. Vanderbilt, Phys. Rev. Lett. 120 (2018) 106403.
[22] Y. Shao, Z. Sun, Y. Wang, C. Xu, R. Sankar, A.J. Breindel, C. Cao, M.M. Fogler, A.J. Millis, F. Chou, et al., Proc. Natl. Acad. Sci. Unit. States Am. 116 (2019) 1168.
[23] T. Bzdušek, Q. Wu, A. Rüegg, M. Sigrist, A.A. Soluyanov, Nature 538 (2016) 75.
[24] H. He, C. Qiu, X. Cai, M. Xiao, M. Ke, F. Zhang, Z. Liu, Nat. Commun. 11 (2020a) 1.
[25] T. Yang, Q. Wan, D. Yan, Z. Zhu, Z. Wang, C. Peng, Y. Huang, R. Yu, J. Hu, Z. Mao, et al., Nat. Mater. 19 (2020b) 27.
[26] C. Shi, R. Zhao, Y. Long, S. Yang, Y. Wang, H. Chen, J. Ren, X. Zhang, Natl. Sci. Rev. 6 (2019) 707.
[27] Y. Long, H. Ge, D. Zhang, X. Xu, J. Ren, M.-H. Lu, M. Bao, H. Chen, Y.-F. Chen, Natl. Sci. Rev. 7 (2020a) 1024.
[28] Y. Long, D. Zhang, C. Yang, J. Ge, H. Chen, J. Ren, Nat. Commun. 11 (2020b) 4716.
[29] C. He, X. Ni, H. Ge, X.-C. Sun, Y.-B. Chen, M.-H. Lu, X.-P. Liu, Y.-F. Chen, Nat. Phys. 12 (2016) 1124.
[30] Z. Zhang, Q. Wei, Y. Cheng, T. Zhang, D. Wu, X. Liu, Phys. Rev. Lett. 118 (2017a): 084303.
[31] Z. Zhang, Y. Tian, Y. Cheng, X. Liu, J. Christensen, Phys. Rev. B 96 (2017b) 241306.
[32] C. He, H.-S. Lai, B. He, S.-Y. Yu, X. Xu, M.-H. Lu, Y.-F. Chen, Nat. Commun. 11 (2020b) 1.
[33] M. Maffei, A. Dauphin, F. Cardano, M. Lewenstein, P. Massignan, New J. Phys. 20 (2018): 013023.
[34] L. Fu, Phys. Rev. Lett. 106 (2011) 106802.